Submitted to *AIAA Journal of Guidance, Control, and Dynamics*

Peak-Seeking Control for Drag Reduction in Formation Flight

David F. Chichka* and Jason L. Speyer†
University of California, Los Angeles, Los Angeles, California, 90095
Claudio Fanti‡
Università di Padova, Padova, Italy
Chan Gook Park§
Kwangwoon University, Seoul, Korea

Abstract

Formation flight is a known method of improving the overall aerodynamic efficiency of a pair of aircraft. In particular, one craft flying in the correct position in the vortex wake of another can realize substantial reductions in drag, with the amount of the reduction dependent on the relative positions of the two craft. This paper looks at such a pair, with one craft flying behind and to the side of the lead plane. The precise position of the second craft relative to the first to maximize the drag reduction is to be determined online, leading to a peak-seeking control problem. A new method of peak-seeking control, using a Kalman filter to estimate the characteristics of the drag reduction, is derived and discussed. A simple model of the two-plane formation using horseshoe vortices is defined, and the peak-seeking controller is applied to this model. The method is demonstrated in simulation using this simplified model.

1 Introduction

As an airplane flies, it causes an upwash ahead of the wing, and leaves a wake behind. This wake is characterized by the downwash behind the wing, and by an accompanying upwash in the area on either side of the downwash region. By flying in the area of upwash, a second aircraft can gain a substantial efficiency boost, due to the reduction in induced drag it will experience. This leads to the well-known fact that two aircraft flying in an appropriate formation can achieve overall efficiency much greater than were they flying separately [1]. This effect is analyzed using inviscid aerodynamic assumptions and lifting-line theory in [2], where it is noted that the effects were considered by Munk as early as 1919. The theory was put to test in actual aircraft by Hummel[3], who established a fifteen per cent reduction on the second of a pair of civilian aircraft.

Due to the gains in efficiency, formation flight has been investigated as a way of increasing the range and duration of autonomous aerial vehicles. In [4, 5], formations of several aircraft are considered, with the object of creating a solar-powered formation that could cruise at high altitude for arbitrarily long times. In [4], decentralized controllers are derived for a formation of five high aspect ratio craft, and are shown to be capable of maintaining a prescribed formation despite the nonlinear, destabilizing moments induced on each plane by the aircraft ahead of it in the formation. The formation maintenance problem for a pair of F-16 class aircraft is considered in [6], though that paper relegates the rolling moments on the trailing craft to an inner-loop controller and considers only the lift and side force in designing an autopilot for the trailing plane.

In this paper, only a pair of aircraft is considered. The two craft may be thought of as a leader and a follower. The leader flies straight and level, as if alone. The second plane flies behind and outboard of the leader, in the upwash pattern on one side (we will take it to be the right hand side, but the analysis is the same for the left side). In this configuration, there is only a negligible effect of the follower on the leader, and it is the follower that gets the direct benefit of reduced drag. The precise position of the follower for maximal drag reduction

*Assistant Research Engineer, Mechanical and Aerospace Engineering. Also Senior Engineer, Control and Dynamical Systems Dept, California Institute of Technology, Pasadena, California. Senior Member, AIAA.

†Professor, Mechanical and Aerospace Engineering. Fellow, AIAA.

‡Visiting Undergraduate Student, Dipartimento di Elettronica ed Informatica, Università di Padova, Padova, Italy

§Associate Professor, Control and Instrumentation Engineering

depends on the flight conditions and the geometries of the actual aircraft involved. For this reason, it is desireable to have a method of identifying the optimal location in flight. When considering unpiloted aerial vehicles (UAVs), it is particularly important that this method be automated.

The general class of such control problems is that of *peak-seeking* control, also referred to as extremum-seeking control. Such problems were addressed as long ago as 1922[7], and are briefly reviewed in [8]. More recently, the topic has been examined in connection with combustion instability in axial-flow compressors [9, 10, 11] and various other applications [12]. The analysis of these problems is addressed in [13], where an averaging framework is suggested.

In the next section, the aerodynamics of formation flight are briefly reviewed, using standard inviscid fluid theory, and a model of the effects of formation flight on the trailing aircraft is derived. The third section presents the peak-seeking scheme to be used to optimize the drag benefit during flight. Simulation results are presented in section 4, and the fifth section concludes the paper.

2 Aerodynamics of Formation Flight

A detailed description of the aerodynamics of even a single aircraft is highly complicated. However, for the purposes of this discussion, most of the details of airflow over an airplane may be ignored. Instead, we take the point of view that the effects of flight on an aircraft, and of the aircraft on the air that flows over it, are principally due to the wing, and the creation of lift. For that reason, we will consider only the wing. Further, we will use the bound vortex model[2, 1] to represent the wing of the leading craft. This will enable a straightforward model that captures the significant effects of formation flight on the trailing craft. It should be noted that this is not intended to be a complete and detailed model of the flow about the trailing craft. Also, because we assume inviscid and incompressible flow, the model loses its validity at near-transonic velocities.

As a further simplifying assumption, we will assume that the lead aircraft maintains straight and level flight at all times.

2.1 Bound Vortex Model

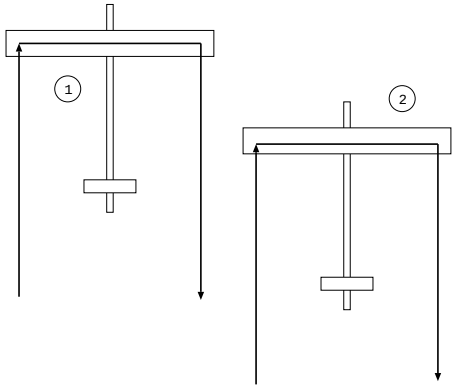

Figure 1: Two aircraft in formation.

Consider two aircraft flying in formation. Each craft is modeled using the horseshoe vortex, as in Figure 1. This is intended to model the effects of the aircraft on the air around it, rather than to carefully model the airflow near the airplane itself. A central assumption in this model is that the effects on the airflow are almost entirely due to the lift generated by the wing.

To calculate these effects, the wing is modeled as a single, straight vortex segment, which is "bound" to the wing. In keeping with the Helmholtz vortex laws, this vortex cannot simply end at the wingtips. Instead, it extends as a semi-infinite vortex from each wingtip. In general, these vortices are not fixed in space, but are free to move with the surrounding airmass. In the horseshoe vortex model, they are assumed to be straight, and under inviscid flow assumptions they lose none of their strength, regardless of how far away the wing becomes.

Remark 1: The vortex wake of an aircraft is of course much more complicated than this. In particular, most wings do not have a single, well-defined vortex from the wingtip. Instead, the vorticity is distributed through the wake behind the entire wing. Also, the wake descends slightly behind the aircraft. However, the majority of the vorticity, particularly from a wing with high aspect ratio, tends to be shed near the tip of the wing. ♣

The velocity induced by a vortex segment on the surrounding inviscid fluid is described by the Biot-Savart law. The situation is shown in Figure 2. In this figure, the velocity induced at the point P by

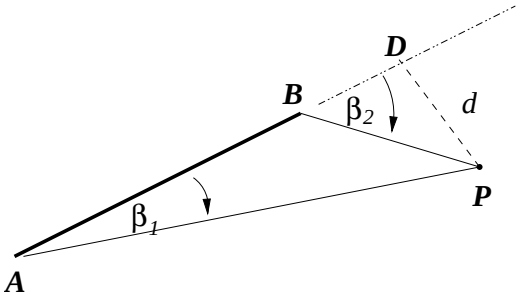

Figure 2: The Biot-Savart law.

the vortex segment running from A to B is given by

$$q = \frac{\Gamma}{4\pi d}\left(\cos\beta_1 - \cos\beta_2\right) \tag{1}$$

where Γ is the strength per unit length of the vortex and d is the shortest distance from P to the line along which the segment lies. The sign of the velocity is positive by the right hand rule about the vortex segment.

Applying this law to a single airplane explains the creation of the upwash ahead of a wing, the downwash behind, and the upwash regions outboard of each trailing vortex. When it is applied to Figure 1, it is easy to see that there is little effect generated by the trailing aircraft on the leader. The upwash generated by the wing's bound vortex, and that of the outboard wingtip vortex, decay too quickly to have any significant effect. And the inboard wingtip vortex of the trailing plane is poorly positioned to have any effect. Similarly, the effect on the follower aircraft is seen to be almost entirely due to the trailing vortex passing near the inboard wingtip. Because of these effects, we will consider only this vortex and its effect on the follower aircraft.

Remark 2: As noted in remark 1, the wake of an aircraft tends to descend as it leaves the wing. One of the results of formation flight is that the upwash ahead of a well-positioned follower tends to lift the portion of the wake that passes near the wing, so that as it passes the wingtip it is very nearly at the same altitude as the leading aircraft's wingtip. ♣

In the formation shown in Figure 1, the follower is entirely in an upwash region. This upwash causes the angle of attack along the wing to be greater than the nominal angle of attack of the aircraft itself, giving greater lift than would be otherwise generated. Because the upwash is inversely proportional to the distance from the vortex, the effect is strongest at the portion of the wing that is nearest the vortex, and falls away sharply with distance. The result is that the majority of the lift induced on the trailing plane occurs near the end of the wing. This causes a strong outward rolling moment on the follower aircraft.

The reduction in induced drag experienced by the follower craft is related to the lift created by the upwash field. Induced drag is a penalty of creating lift; the gain in efficiency may be thought of as result of the follower not having to create the lift itself, and therefore not creating as much drag. The actual effect can be related to less downwash behind the wing [14, 15]. Hummel[3] relates it to the lift vector on the wing itself, which is rotated forward due to the upwash. For our purposes it is enough to note that the gain in efficiency is related to the gain in lift. Thus, we can exchange the problem of minimizing drag with that of maximizing the vortex-induced lift on the follower craft.

Remark 3: A further effect of the upwash pattern on the follower wing is that the reduction in drag is greater near the end of the wing. This induces a small outward yawing moment on the follower craft. This is a minor effect. ♣

Remark 4: Any side force induced on the follower is assumed negligible, and will not be considered here. ♣

The Kutta-Joukowski Theorem: The strength of the vortices in the problem will be calculated using the Kutta-Joukowski theorem. This theorem deals with the forces induced on a vortex fixed in space, due to the motion of the surrounding fluid. Without derivation, the theorem can be presented as

$$\vec{F} = \rho\vec{V} \times \vec{\Gamma} \tag{2}$$

where ρ is the density of the fluid, $\vec{V}$ is the velocity of the fluid, and $\vec{\Gamma}$ is the strength per unit length of the bound vortex. The resulting force vector $\vec{F}$ is the force per unit length, imposed on the bound vortex. Applying this theorem to an aircraft in steady flight allows the computation of the strength of the bound vortex as

$$\begin{aligned} L &= \rho V_\infty \Gamma b = W \\ &\Rightarrow \quad \Gamma = W/\rho V_\infty b \end{aligned} \tag{3}$$

where L is the lift generated by the bound vortex, W the weight of the aircraft, V_∞ the velocity of the

craft through the fluid, and b the wingspan of craft. Thus the vortex strength is defined by the aircraft parameters and the default flight condition.

2.2 Computation of Induced Lift and Moment

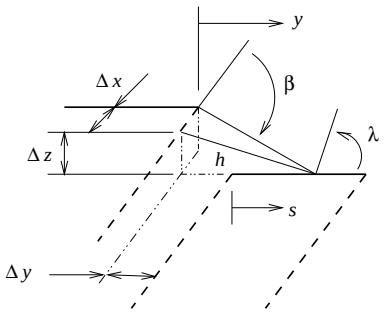

Figure 3: The induced velocity at the trailing wing.

The facts and assumptions of the last section will now be applied to the formation flight problem described earlier. The geometry of the problem is shown in Figure 3. The variables $\Delta x, \Delta y$, and Δz describe the location of the inboard wingtip of the trailing aircraft in relation to the outboard tip of the leader's wing; $\Delta x = \Delta y = \Delta z = 0$ results in the wingtips being aligned. The (constant) velocity of the lead plane is in the x direction, and the straight trailing vortex lies along the x-axis.

We make three further simplifying assumptions. Due to the geometry of the situation, it is easy to see that a small change in following distance makes very little difference in the effects on the trailing plane; thus, we take this distance to be constant. For similar reasons, we take the trailing craft roll angle to be zero at all times, and ignore any effect of sideslip.

Under these assumptions, the problem reduces to computing the effects of a fixed vortex of known strength on the trailing wing. We do this by computing the upwash along the wing using the Biot-Savart law, and from this computing the local angle of attack due to upwash. Assuming a linear relation of lift to angle of attack, this allows the effects due to the presence of the vortex to be added to the lift and moment generated by the orientation of the aircraft itself. Denoting the induced lift at a point on the wing as $\Delta L(s)$, we have the relation

$$d\Delta L(s) = \frac{\rho V_\infty^2 c(s)}{2} C_{l_\alpha}(s) \Delta\alpha(s) ds \tag{4}$$

Here, we use s to mean the point along the wing, with $s = 0$ being the inboard wingtip and $s = b$ the outboard wingtip. The incremental rolling moment induced is simply the incremental lift times the moment arm, giving

$$dM(s) = d\Delta L(s)(b/2 - s) ds \tag{5}$$

The induced angle of attack we will compute as

$$\Delta\alpha(s) = \tan^{-1}(w/V_\infty) \approx w/V_\infty \tag{6}$$

where w is the upwash velocity induced by the trailing vortex. We can compute this as $w = q \sin\lambda$, where λ is defined as in Figure 3.

We can represent λ through the geometry of the situation as

$$\sin\lambda = \cos(\pi/2 - \lambda) = \frac{y}{\sqrt{y^2 + \Delta z^2}} \tag{7}$$

with the distance h as

$$h = \sqrt{y^2 + \Delta z^2} \tag{8}$$

The values of the cosines in (1) become

$$\begin{aligned} \cos\beta_1 &= \frac{\Delta x}{\sqrt{\Delta x^2 + \Delta z^2 + (\Delta y + s)^2}} \\ \cos\beta_2 &= -1 \end{aligned} \tag{9}$$

Combining (7), (8), (9), and the Biot-Savart law gives

$$w(y) = q \sin\lambda = \frac{\Gamma}{4\pi} \frac{y}{y^2 + \Delta z^2} \times \left(1 + \frac{\Delta x}{\sqrt{\Delta x^2 + \Delta z^2 + (\Delta y + s)^2}}\right) \tag{10}$$

Assembling all of these results, we arrive at the expressions

$$\Delta L = \frac{\rho V_\infty \Gamma}{8\pi} C_{L_\alpha} \int_0^b \frac{y}{y^2 + \Delta z^2} \times \left(1 + \frac{\Delta x}{\sqrt{\Delta x^2 + \Delta z^2 + (\Delta y + s)^2}}\right) ds \tag{11}$$

and

$$\Delta M = \frac{\rho V_\infty \Gamma}{8\pi} C_{L_\alpha} \int_0^b \frac{y}{y^2 + \Delta z^2} \times \left(1 + \frac{\Delta x}{\sqrt{\Delta x^2 + \Delta z^2 + (\Delta y + s)^2}}\right) (b/2 - s) ds \tag{12}$$

where the lift curve slope has been assumed constant for all s. For rectangular wings, the chord $c(s)$ is also constant, allowing further simplification.

The Vortex Core: The Biot-Savart result used so far becomes meaningless when the wingtip of the trailing aircraft approaches the core of the vortex. When $\Delta z = 0$ and $\Delta y + s = 0$ is included in the integration interval, in fact, the integral of ds/s is clearly unbounded and so would be the lift generated.

To deal with this, we note that the vortex core has finite diameter. Within this core, the velocity is often assumed to be linear with distance from the center of the core, and this will be assumed here. We can further simplify the equations by noting that Δx always has some appreciable value, while within the core y and Δz must both be small. Therefore, we take the value of $\cos\beta_1$ in this region to be 1. Combining these assumptions, the upwash within the core becomes simply

$$\overline{w} = k\sqrt{y^2 + \Delta z^2} \tag{13}$$

where the constant k will be chosen such the upwash is constant across the boundary of the vortex core, and the expressions for ΔL and ΔM become much simpler.

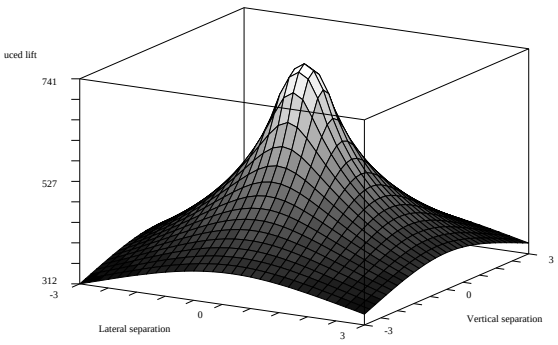

Figure 4: Induced lift.

The induced lift as a function of lateral and vertical separation is shown in Figure 4. A zero value of separation refers to wingtips aligned. The values are taken from [16] for a Cessna-172 type aircraft. The vortex core radius was chosen such that at the edge of the core, the induced angle of attack is approximately 12 degrees; above this value, the total angle of attack is such that the wing would most likely stall. The actual values used are given later in this paper, when the simulation is discussed.

2.3 Effects of Wing Geometry and Follower Position

While the topic of this paper is control rather than aerodynamics, a few comments on the effects of wing geometry and follower position are in order. The effect of the second of these is straightforward; the effect of the first is less so. In both cases, the effects are due to the combination of upwash outboard of the leading wing's vortex wake, and the strong downwash just inside.

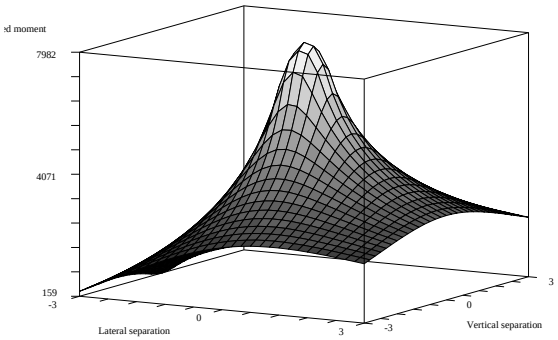

Figure 5: Induced moment function.

First consider an aircraft with a rectangular wing, such as sketched in Figure 1, and let the trailing vortex from the leader be fixed in space (let the vortex have some finite diameter, so that the induced velocities remain finite). As the follower craft gets farther from the vortex, both the lift and moment induced on it go to zero. As it comes closer, both lift and moment increase, until both are maximized as the wingtip touches the vortex. Should the follower continue inward, so that its wingtip is now in the downwash field, both lift and moment begin to decrease. This is because the downwash creates a downward force on the wing, and thus a moment in the opposite direction to that imposed on the rest of the wing. As this section has the greatest moment arm, the reduction in moment is larger (in proportion to the overall induced moment) than is the reduction in lift. This asymmetry can be seen near the vortex by comparing the moment function displayed in

Figure 5 with the lift function in Figure 4. As more of the wing enters the downwash area, there comes a point at which there is still positive induced lift, while the moment goes to zero. The extreme case occurs when the vortex runs down the centerline of the follower craft. Were this case physically possible, it would result in zero overall induced lift, while a moment rolling the follower into the leader's wake would be at maximum strength.

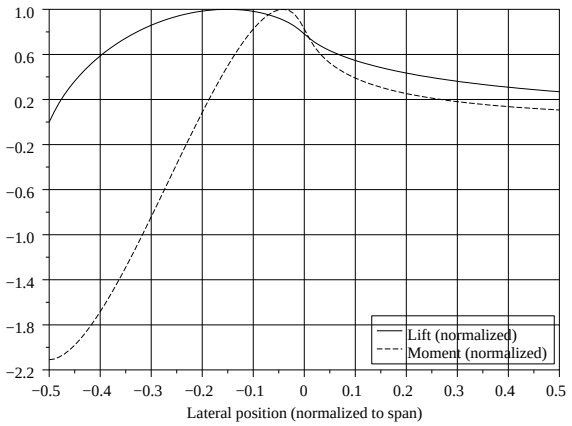

Figure 6: Normalized lift and moment vs. lateral position for a delta wing.

If we replace the rectangular wing on the follower craft with a delta wing, the effects on the follower become less straightforward. In this case, a small overlap of the follower craft, so that a wingtip is in the downwash region, might be desireable. This is because the area of the wing section in downwash is small, while the part of the wing now in the strong upwash section has a larger chord (consider eqn. 4). Therefore, the net effect is a gain in lift. The greater moment arm of the section in the downwash region exaggerates the effect on the total induced moment, however. Because of this, the moment will begin to decrease even as the lift continues to increase with overlap. This effect is illustrated in Figure 6, which shows the effect on a trailing aircraft with a delta wing. The lateral position varies from $-b/2$, so that the vortex runs down the follower centerline, to $b/2$. Note that the point of maximum induced lift coincides with an overlap of approximately $0.15b$, while the maximum induced moment remains near zero overlap.

Because many aircraft have at least some taper to their wings, even in this simplified analysis the optimal flight formation would include some overlap. When the effect of a distributed vortex wake from a leading craft with wing taper is included, the overlap for maximum lift may be quite high.

Remark 5: All of the analysis in this paper ignores the changes in lift distribution on the follower aircraft wing due to control deflections. It is known[3], that this can have an effect on the drag reduction (Hummel reports an enhancement). However, this effect is specific to particular aircraft, and will not be addressed here. It may be taken as a further reason that the precise position for greatest drag reduction is unlikely to be known in advance. ♣

3 Peak Seeking Scheme

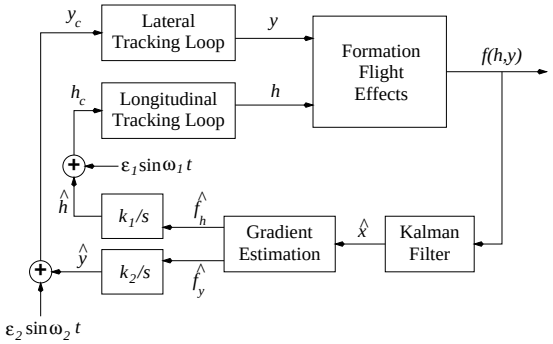

Figure 7: Block diagram of peak-seeking controller.

The physical problem having been defined, we proceed to derive a controller to maximize the lift during flight. As demonstrated, the lift is primarily a function of the lateral and vertical separation of the aircraft, and as modeled this is specifically true. Thus, we seek a controller that optimizes on-line a nonlinear function of the system states Δy and Δz. The structure of the resulting controller will be as shown in Figure 7.

The peak-seeking scheme begins with the proposition that the current value of the states is the optimum. Were this true, the control system would be primarily concerned with maintaining these values; this is the usual disturbance-rejection task. To find out if it is true, a dither signal is added to each of the states of interest. The aircraft tracks these oscillating states, and the resulting motion of the aircraft results in an oscillation in the value of the function

to be maximized (in this case the drag benefit of formation flight).

The value of the function is fed to a modified Kalman filter, which is used to estimate the values of the gradients of the function with respect to the states of interest. These estimated gradients are used as input for the controller, which in turn yields what is taken to be the optimal value of the states. The dither signal is again added, and the loop continues. In this way, the states are adjusted until the gradient estimate goes to zero. In most earlier work (for example [9]), only the sign of the estimated gradient is used in the peak-seeking loop; to the authors' knowledge, the first use of the gradient estimate itself in the loop is presented in [20].

We will first derive a Kalman filter to be used to derive the gradient, and then implement a control loop that includes the filter.

3.1 Kalman Filter for Gradient Estimation

Because we are assuming straight and level flight on the part of the lead aircraft, we may ignore that craft in deriving the filter and the controller. Therefore, we will define the function to be maximized as a function of the trailing aircraft states only. In this section, we use h to denote the altitude of the aircraft, rather than $-z$. The variable z is taken to be the measurement of the linear system under consideration.

We begin by expanding the function to be extremized as

$$f(h,y) = f(\hat{h},\hat{y}) + f_h(\hat{h},\hat{y})\delta h + f_y(\hat{h},\hat{y})\delta y + o(\delta h, \delta y) \tag{14}$$

where $(\hat{h},\hat{y})$ is the current estimate. Introducing the dither signals into the input of the tracking loop (see Figure 7), the output is assumed to first-order to be

$$h \cong \hat{h} + \delta h = \hat{h} + \bar{\varepsilon}_1 \sin(\omega_1 t + \theta_1) \tag{15}$$

$$y \cong \hat{y} + \delta y = \hat{y} + \bar{\varepsilon}_2 \sin(\omega_2 t + \theta_2) \tag{16}$$

The underlying assumptions are that the gradient changes are slow with respect to the tracking loops and the dither frequencies, so that $\hat{h}$ and $\hat{y}$ may be assumed constant, and that the dither inputs are tracked well, except for an amplitude and phase uncertainty. Under these assumptions, the expansion (14) of the formation flight effects becomes

$$\begin{aligned} f(h,y) =& f(\hat{h},\hat{y}) + \bar{\varepsilon}_1 f_h(\hat{h},\hat{y})\sin(\omega_1 t + \theta_1(t)) \\ &+ \bar{\varepsilon}_2 f_y(\hat{h},\hat{y})\sin(\omega_2 t + \theta_2(t)) + o(\delta h, \delta y) \end{aligned} \tag{17}$$

where $\varepsilon_{()}$ and $\omega_{()}$ of the input dither signal are to be chosen by the designer.

To estimate the two gradients using the Kalman filter, we define the state variables

$$x \equiv \begin{bmatrix} x_1 \\ x_2 \\ x_3 \\ x_4 \\ x_5 \end{bmatrix} = \begin{bmatrix} \tilde{f}_h \sin(\omega_1 t + \theta_1) \\ \tilde{f}_h \cos(\omega_1 t + \theta_1) \\ \tilde{f}_y \sin(\omega_2 t + \theta_2) \\ \tilde{f}_y \cos(\omega_2 t + \theta_2) \\ f(\hat{h},\hat{y}) \end{bmatrix} \tag{18}$$

where $\tilde{f}_h = \bar{\varepsilon}_1 f_h(\hat{h},\hat{y})$ and $\tilde{f}_y = \bar{\varepsilon}_2 f_y(\hat{h},\hat{y})$. We act for now as if the pair $(\hat{h},\hat{y})$ were fixed, so that f, f_h, and f_y may be treated as unknown constants. Furthermore, we assume that θ_1 is a Brownian motion process with zero mean and variance $E[\theta_1(t)\theta_1(\tau)] = \sigma_1^2 t$ if $\tau \geq t$ (with similar assumptions on θ_2). This fits the theory given in [19]. If the Îto differentials of x are taken, then we get

$$dx = Fxdt + dGx + dw \tag{19}$$

where

$$F = \begin{bmatrix} -\frac{\sigma_1^2}{2} & \omega_1 & 0 & 0 & 0 \\ -\omega_1 & -\frac{\sigma_1^2}{2} & 0 & 0 & 0 \\ 0 & 0 & -\frac{\sigma_2^2}{2} & \omega_2 & 0 \\ 0 & 0 & -\omega_2 & -\frac{\sigma_2^2}{2} & 0 \\ 0 & 0 & 0 & 0 & \kappa \end{bmatrix};$$

$$dG = \begin{bmatrix} 0 & d\theta_1 & 0 & 0 & 0 \\ -d\theta_1 & 0 & 0 & 0 & 0 \\ 0 & 0 & 0 & d\theta_2 & 0 \\ 0 & 0 & -d\theta_2 & 0 & 0 \\ 0 & 0 & 0 & 0 & 0 \end{bmatrix};$$

$$dw = [0 \quad 0 \quad 0 \quad 0 \quad dw_0]^T$$

$w_0(t)$ is a white Gaussian process noise with zero mean and spectral density W_0, and the values for $\sigma_1, \sigma_2, \kappa$, and W_0 are empirically determined through simulation and filter performance.

Allowing the higher-order terms in eqn. (17) to be considered as noise, the measurement equation is expressed as:

$$\begin{aligned} z(t) &= [1 \quad 0 \quad 1 \quad 0 \quad 1]x(t) + v(t) \\ &= Hx(t) + v(t) \end{aligned} \tag{20}$$

where $v(t) \sim N(0, V(t))$, and $z(t)$ recovers $f(\hat{h}, \hat{y})$.

The filter for the above dynamic structure (19,20) is taken to be the best linear minimum variance estimator as

$$\dot{\hat{x}} = F\hat{x} + K(z - \hat{z}) \tag{21}$$

where

$$K = PH^T V^{-1} \tag{22}$$

and P satisfies the Riccati equation

$$\dot{P} = FP + PF^T + \Delta(X) + W - PH^T V^{-1} HP \tag{23}$$

where X is the variance of x taken here to be in steady state, X_{ss}. Therefore, the sum $\Delta(X_{\text{ss}}) + W$ where W is the variance of the additive noise is

$$\Delta(X_{\text{ss}}) + W = \begin{bmatrix} \sigma_1^2 & 0 & 0 & 0 & 0 \\ 0 & \sigma_1^2 & 0 & 0 & 0 \\ 0 & 0 & \sigma_2^2 & 0 & 0 \\ 0 & 0 & 0 & \sigma_2^2 & 0 \\ 0 & 0 & 0 & 0 & W_0 \end{bmatrix} \tag{24}$$

The estimates of state associated with altitude are

$$\begin{aligned} \hat{x}_1 &= \tilde{f}_h \sin\widehat{(\omega_1 t + \theta)} \\ \hat{x}_2 &= \tilde{f}_h \cos\widehat{(\omega_1 t + \theta)} \end{aligned} \tag{25}$$

We can obtain the magnitude of the gradient as

$$|\hat{\tilde{f}}_h| = \sqrt{\hat{x}_1^2 + \hat{x}_2^2} \tag{26}$$

Combining eqn. (25) and eqn. (26), the gradient $\tilde{f}_h$ is estimated as

$$\hat{\tilde{f}}_h = \sqrt{\hat{x}_1^2 + \hat{x}_2^2}\, \text{sgn}(\hat{x}_1 \sin\omega_1 t + \hat{x}_2 \cos\omega_1 t) \tag{27}$$

Similarly, the gradient $\tilde{f}_y$ is computed as

$$\hat{\tilde{f}}_y = \sqrt{\hat{x}_3^2 + \hat{x}_4^2}\, \text{sgn}(\hat{x}_3 \sin\omega_2 t + \hat{x}_4 \cos\omega_2 t) \tag{28}$$

Note that due to the signum function, the gradient estimates are not necessarily continuous. Note also that $\bar{\varepsilon}_1$ and $\bar{\varepsilon}_2$ are embedded in eqns. (27,28). Their effect is compensated by the values of the gains k_1 and k_2 chosen in the peak-seeking loop in Figure 7.

3.2 Sinusoidal Tracking Loop for Aerodynamics

For the purpose of control system design, the aircraft's dynamics are frequently linearized about some operating condition or flight regime. The control surfaces and engine thrust are trimmed at these conditions and the control system is designed to maintain them, i.e., to force any perturbation from these conditions to zero.

Also, it is customary to separate the longitudinal motion from the lateral motion in studying small perturbations from trim conditions. In most cases the lateral and longitudinal dynamics are only lightly coupled, and the control system can be designed for each channel without regard to the other [17]. This approach is taken in this work, so that the longitudinal and lateral tracking loops are designed separately. The state vectors, plant, and control matrices used are as follows:

• Longitudinal Dynamics

$$\begin{bmatrix} \dot{s} \\ \dot{\alpha} \\ \dot{q} \\ \dot{\theta} \\ \dot{h} \end{bmatrix} = \begin{bmatrix} X_s & X_\alpha & 0 & -g & 0 \\ Z_{sV} & Z_{\alpha V} & 1 & 0 & 0 \\ M_s & M_\alpha & M_q & 0 & 0 \\ 0 & 0 & 1 & 0 & 0 \\ 0 & -V & 0 & V & 0 \end{bmatrix} \begin{bmatrix} s \\ \alpha \\ q \\ \theta \\ h \end{bmatrix} + \begin{bmatrix} X_E \\ Z_{EV} \\ M_E \\ 0 \\ 0 \end{bmatrix} \delta_E + \begin{bmatrix} \alpha \\ -1/V \\ 0 \\ 0 \\ 0 \end{bmatrix} \bar{L} \tag{29}$$

where

s	=	Change in speed	(ft/sec)
α	=	Angle of attack	(rad)
q	=	Pitch rate	(rad/sec)
θ	=	Pitch angle	(rad)
h	=	Altitude	(ft)
δ_E	=	Elevator deflection	(rad)

• Lateral Dynamics

$$\begin{bmatrix} \dot{\beta} \\ \dot{p} \\ \dot{r} \\ \dot{\phi} \\ \dot{\psi} \\ \dot{y} \end{bmatrix} = \begin{bmatrix} Y_{\beta V} & Y_{pV} & Y_{rV} - 1 & gV & 0 & 0 \\ L_\beta & L_p & L_r & 0 & 0 & L_y \\ N_\beta & N_p & N_r & 0 & 0 & 0 \\ 0 & 1 & 0 & 0 & 0 & 0 \\ 0 & 0 & 1 & 0 & 0 & 0 \\ -V & 0 & 0 & 0 & V & 0 \end{bmatrix} \times \begin{bmatrix} \beta \\ p \\ r \\ \phi \\ \psi \\ y \end{bmatrix} + \begin{bmatrix} Y_{AV} & Y_{RV} \\ L_A & L_R \\ N_A & N_R \\ 0 & 0 \\ 0 & 0 \\ 0 & 0 \end{bmatrix} \begin{bmatrix} \delta_A \\ \delta_R \end{bmatrix} + \begin{bmatrix} 0 \\ 1 \\ 0 \\ 0 \\ 0 \\ 0 \end{bmatrix} \bar{L}_u \tag{30}$$

where

β	=	Slide slip angle	(rad)
p	=	Roll rate	(rad/sec)
r	=	Yaw rate	(rad/sec)
ϕ	=	Roll angle	(rad)
ψ	=	Yaw angle	(rad)
y	=	Cross-track displacement	(ft)
δ_A	=	Aileron deflection	(rad)
δ_R	=	Rudder deflection	(rad)

Note the additions to the usual linear aircraft equations. The longitudinal channel includes an additional input to the $\dot{\alpha}$ equation, due to the vortex-induced lift. For the same of controller design, this is modelled as a constant input. The lateral channel (eqn. 30) includes both a constant term and a linearly-varying term in the $\dot{p}$ equation, this time due to the vortex-induced rolling moment.

Because the command input of the system is oscillatory, eqns. (29,30) cannot be used directly to derive the controllers. First, an error state must be developed that maps the oscillatory system into a linear space, in which the system does not appear oscillatory. Standard Linear Quadratic Regulator (LQR) techniques may then be used to derive the controller. Note that, for state space, a similar approach was seen in [17]. The design process for the controller for the longitudinal states will be covered briefly here.

First, an error state is defined as

$$e = h_c - h \tag{31}$$

and, taking derivatives and substituting values from eqn. (29), this leads to the equations

$$\begin{aligned} e_1 = e &= h_c - h = \hat{h} + \varepsilon_1 \sin\omega_1 t - h \\ e_2 &= \dot{e}_1 = \dot{h}_c - \dot{h} = \omega_1 \varepsilon_1 \cos\omega_1 t - V(\theta - \alpha) \\ e_3 &= \dot{e}_2 = -\omega_1^2 \varepsilon_1 \sin\omega_1 t - V(\dot{\theta} - \dot{\alpha}) \end{aligned}$$

Now, this third error state has the derivative

$$\dot{e_3} = -\omega_1^2 e_2 + V(\omega_1^2\alpha + \ddot{\alpha}) - V(\omega_1^2\theta + \ddot{\theta})$$

The repetition of terms such as $\omega_1^2\alpha + \ddot{\alpha}$ leads us to introduce the new state

$$\bar{\theta} = \omega_1^2\theta + \ddot{\theta}$$

which has the derivative

$$\dot{\bar{\theta}} = \omega_1^2\dot{\theta} + \theta^{(3)} = \omega_1^2 q + \ddot{q}$$

Following in this pattern, we introduce the states

$$\begin{aligned} \bar{\alpha} &= \omega_1^2\alpha + \ddot{\alpha} \\ \bar{s} &= \omega_1^2 s + \ddot{s} \\ \bar{q} &= \omega_1^2 q + \ddot{q} \end{aligned}$$

and the control variable

$$\bar{\delta}_E = \omega_1^2\delta_E + \ddot{\delta}_E \tag{32}$$

Using these states and control, the dynamic system from eqn. (29) becomes

$$\begin{bmatrix} \dot{e_1} \\ \dot{e_2} \\ \dot{e_3} \\ \dot{\bar{s}} \\ \dot{\bar{\alpha}} \\ \dot{\bar{q}} \\ \dot{\bar{\theta}} \end{bmatrix} = \begin{bmatrix} 0 & 1 & 0 & 0 & 0 & 0 & 0 \\ 0 & 0 & 1 & 0 & 0 & 0 & 0 \\ 0 & -\omega^2 & 0 & 0 & V & 0 & -V \\ 0 & 0 & 0 & X_s & X_\alpha & 0 & -g \\ 0 & 0 & 0 & Z_{sv} & Z_{\alpha V} & 1 & 0 \\ 0 & 0 & 0 & M_s & M_\alpha & M_q & 0 \\ 0 & 0 & 0 & 0 & 0 & 1 & 0 \end{bmatrix} \times \begin{bmatrix} e_1 \\ e_2 \\ e_3 \\ \bar{s} \\ \bar{\alpha} \\ \bar{q} \\ \bar{\theta} \end{bmatrix} + \begin{bmatrix} 0 \\ 0 \\ 0 \\ X_E \\ Z_E \\ M_E \\ 0 \end{bmatrix} \bar{\delta}_E \tag{33}$$

Note that the new control variable $\bar{\delta}_E$ is not oscillatory; a glance at eqn. (32) shows that the actual control δ_E will, however, have the desired sinusoidal characteristics.

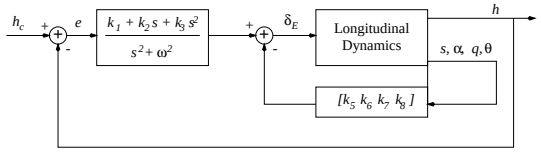

Figure 8: Longitudinal Channel Controller

Now that a standard linear system has been derived, standard LQR techniques quickly provide a stable controller for this system. Converting the states and control back to the original state space results in a controller of the form in Figure 8.

For the lateral dynamics we have:

$$\begin{bmatrix} \dot{e_1} \\ \dot{e_2} \\ \dot{e_3} \\ \dot{e_4} \\ \dot{\bar{\beta}} \\ \dot{\bar{p}} \\ \dot{\bar{r}} \\ \dot{\bar{\phi}} \\ \dot{\bar{\psi}} \\ \dot{\bar{\xi}} \end{bmatrix} = \begin{bmatrix} 0 & 1 & 0 & 0 & 0 \\ 0 & 0 & 1 & 0 & 0 \\ 0 & 0 & 0 & 1 & 0 \\ 0 & 0 & -\omega^2 & 0 & V \\ 0 & 0 & 0 & 0 & Y_{\beta V} \\ 0 & -\omega L_y & 0 & -L_y & L_\beta \\ 0 & 0 & 0 & 0 & N_\beta \\ 0 & 0 & 0 & 0 & 0 \\ 0 & 0 & 0 & 0 & 0 \\ 0 & 0 & 0 & 0 & 0 \end{bmatrix} \cdots$$

$$\cdots \begin{bmatrix} 0 & 0 & 0 & 0 & 0 \\ 0 & 0 & 0 & 0 & 0 \\ 0 & 0 & 0 & 0 & 0 \\ 0 & 0 & 0 & -V & 0 \\ Y_{pV} & Y_{rV}-1 & g_V & 0 & 0 \\ L_p & L_r & 0 & 0 & 0 \\ N_p & N_r & 0 & 0 & 0 \\ 1 & 0 & 0 & 0 & 0 \\ 0 & 1 & 0 & 0 & 0 \\ 0 & 0 & 1 & 0 & 0 \end{bmatrix} \begin{bmatrix} e_1 \\ e_2 \\ e_3 \\ e_4 \\ \bar{\beta} \\ \bar{p} \\ \bar{r} \\ \bar{\phi} \\ \bar{\psi} \\ \bar{\xi} \end{bmatrix}$$

$$+ \begin{bmatrix} 0 & 0 \\ 0 & 0 \\ 0 & 0 \\ 0 & 0 \\ Y_{AV} & Y_{RV} \\ L_A & L_R \\ N_A & N_R \\ 0 & 0 \\ 0 & 0 \\ 0 & 0 \end{bmatrix} \begin{bmatrix} \bar{\delta}_A \\ \bar{\delta}_R \end{bmatrix} \tag{34}$$

where

$$\begin{aligned} e_1 &= y_c - y; \qquad y_c = y_0 + \varepsilon \sin \omega t \\ e_2 &= \dot{e_1}; \qquad e_3 = \dot{e_2}; \qquad e_4 = \dot{e_3} \\ \bar{\beta} &= \omega^2 \dot{\beta} + \beta^{(3)} \\ \bar{p} &= \omega^2 \dot{p} + p^{(3)} \\ \bar{r} &= \omega^2 \dot{r} + r^{(3)} \\ \bar{\phi} &= \omega^2 \dot{\theta} + \theta^{(3)} = \dot{\xi} \\ \bar{\psi} &= \omega^2 \dot{\psi} + \psi^{(3)} \\ \xi &= \omega^2 \theta + \phi^{(3)} \\ \bar{\delta}_A &= \omega^2 \dot{\delta}_A + \delta_A^{(3)} \\ \bar{\delta}_R &= \omega^2 \dot{\delta}_R + \delta_R^{(3)} \end{aligned}$$

and again, LQR techniques provide a stable controller for the system. In these dynamics, the rolling moment due to the vortex is included, as it is a very strong term. This led to the need for one higher level of differentiation in the error states.

3.3 Peak-Seeking Loop

The controller derived in the preceding section assumes a constant value to track, in keeping with the assumption that the estimate of the optimal flight position changes slowly. Note that this assumption is inherent in the time-scale separation that allows a dither signal to be imposed on a "constant" nominal value of $(\hat{y}, \hat{h})$ in the Kalman filter.

Given that the initial assumption of $(\hat{y}, \hat{h})$ is bound to be incorrect, we must have a way to update it. In some earlier work[10], where only the sign of the gradient was found, this was done merely by integrating a constant times the sign of the estimated gradient. Later[20], this was extended to integrating a multiple of the gradient estimate itself. The second approach will be used here, giving an overall control loop as shown in Figure 7.

4 Simulation Results

In this section, we apply the peak-seeking controller derived in section 3 to the formation flight problem. Rather than attempt to minimize drag directly, we instead maximize the rolling moment induced by the vortex from the lead craft. Recall that for the aircraft geometry under consideration, this maximum corresponds to the maximum induced lift. While drag is difficult if not impossible to measure directly, the induced moment can easily be estimated through its effects on the aircraft dynamics. We assume for this simulation that the moment can be effectively measured.

For the puposes of simulation, the lift and moment induced by the vortex are computed as in section 2.2, and added to a linear aircraft model. The model chosen is aircraft "A" from [16], which is much like the Cessna-172 private aircraft. The aircraft parameters and nominal flight condition are given as

$$V_\infty = 219\,\text{ft/sec}, \quad h = 5000\,\text{ft}, \quad \rho = 0.002050\,\text{sl/ft}^3$$

$$W = 2645\,\text{lb}. \quad b = 35.8\,\text{ft} \quad c = 4.9\,\text{ft}$$

Using eqn. (3), this provides the strength per unit length for all vortices to be

$$\Gamma = \frac{2645}{219(0.00205)(35.8)} = 164.6\,\text{ft}^2/\,\text{sec}$$

We are also given a lift coefficient slope for the aircraft. This is an overall coefficient; the airfoil slope is likely to be higher. The theoretical C_{L_α} for any thin airfoil is 2π per radian; experience indicates that a value of about 5.5 per radian is more accurate. The listed overall C_{L_α} of 4.6 is somewhat less. As the upwash affects primarily the airfoil, a value of 5.5 is reasonable. All other values are as given in [16].

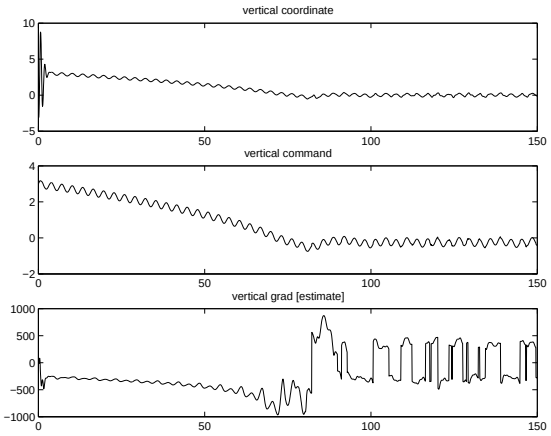

Figure 9: Results for altitude channel.

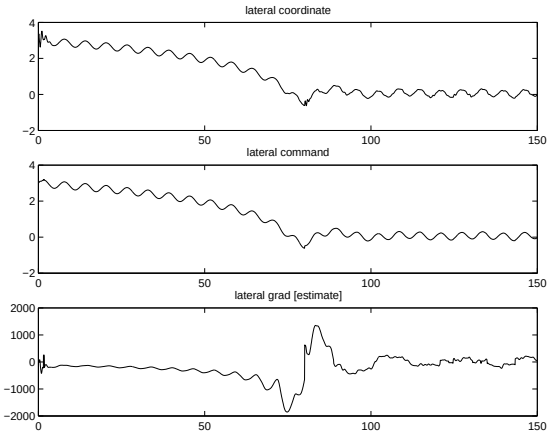

Figure 10: Results for lateral channel.

Time histories from a simulation with initial condition $(h(0), y(0)) = (3, 3)$ are given. The optimal position for this geometry is $(0, 0)$. The initial estimate of the optimal position is, however, the initial condition. The gradient estimates are initialized to zero, and the moment estimate is initialized to the initial measurement of the moment. This set of results is generated assuming zero error in the measurement of the induced moment. The dither frequencies ω_1 and ω_2 are 1Hz and 2Hz, respectively.

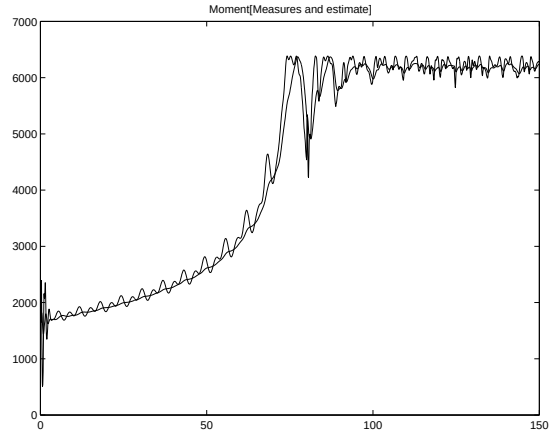

Figure 11: Moment and moment estimate vs. Time.

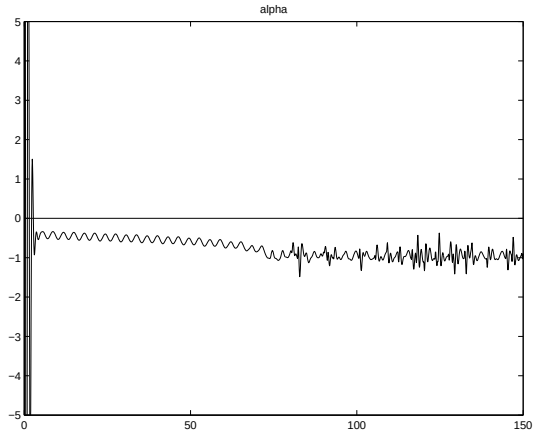

Figure 12: Angle of attack vs. Time.

The position, command, and gradient estimates are presented for the vertical channel in Figure 9, and for the lateral channel in Figure 10. The control commands and the coordinates show the expected oscillatory nature. The craft converges to the optimal position in approximately 80 seconds, after which the gradient estimates oscillate about zero. Note the discontinuous nature of the estimate in the vertical channel; this can be traced to the signum function in the estimate calculation.

The estimated and actual values of the moment are plotted in Figure 11. The effect of both dither signals on the moment can be seen in the oscillating measured moment. The moment estimate tracks

the actual moment well, with the expected slight delay. The best indication of the benefits of formation flight is in Figure 12, which shows the angle of attack. After the expected initial gradients, α is seen to steadily decrease, finally hovering around a value of nearly -1. This represents a reduction in the body angle of attack away from the nominal, caused by the additional lift from the lead aircraft vortex. This is due to the need to generate less lift through body angle, and implies a corresponding reduction in induced drag.

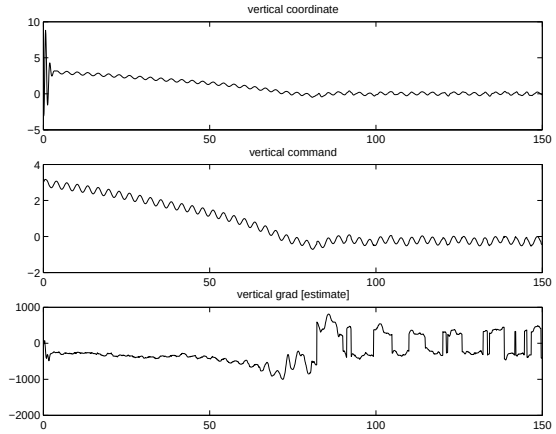

Figure 13: Results for altitude channel, with measurement noise.

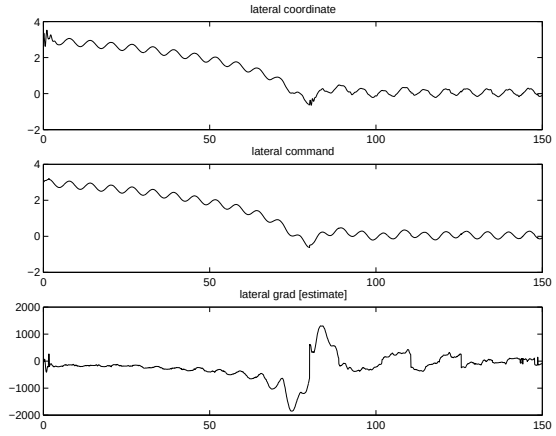

Figure 14: Results for lateral channel, with measurement noise.

The vertical channel results for the same case with a noisy moment measurement are shown in Figure 13, and the lateral channel in Figure 14. The noise is zero mean, with covariance 100. In both

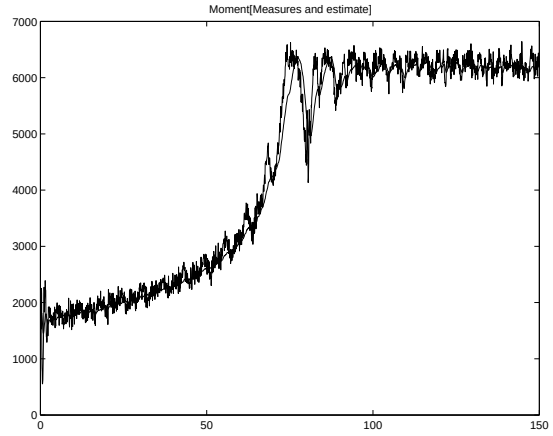

Figure 15: Moment and moment estimate, with measurement noise.

cases, the results are very similar to those without noise. The moment measurement and estimate are displayed in Figure 15. As expected, the convergence is slightly delayed, but the tracking and performance are only slightly degraded.

5 Conclusions

In this paper, an improved peak seeking scheme using modern estimation techniques is proposed. By employing a Kalman filter, the scheme rejects noise systematically, and allows the estimate of the gradients as well as the sign to be used. The technique is applied to a simplified aircraft drag reduction problem, using realistic aircraft dynamics and including the dominant nonlinear terms due to the aircraft interaction. In simulation, the controller readily finds and maintains the optimal position for drag reduction in a two-aircraft formation.

Acknowledgments

This work was supported by the NASA Dryden Flight Research Center under contract number NAS4-00051. Further support was provided by the Air Force Office of Scientific Research under grant number F49620-96-1-0471, administered by the California Institute of Technology.

References

[1] E. L. Houghton and P. W. Carpenter, *Aerodynamics for Engineering Students,* Fourth Edition, John Wiley and Sons, New York, NY, 1993.

[2] Prandtl and Tietjens, *Applied Hydro- and Aeromechanics,* Dover, New York, NY, 1957. (Reprint of 1934 edition.)

[3] D. Hummel, "The Use of Aircraft Wakes to Achieve Power Reductions in Formation Flight", in *The Characterisation & Modification of Wakes from Lifting Vehicles in Fluids*, AGARD Conference Proceedings 584, The Advisory Group for Aerospace Research and Development, 7 Rue Ancelle, 92200 Neuilly-sur-Seine, France, 1996.

[4] J. D. Wolfe, D. F. Chichka, and J. L. Speyer, "Decentralized Controllers for Unmanned Aerial Vehicle Formation Flight", AIAA Paper 96-3833, presented at the AIAA Guidance, Navigation, and Control Conference, San Diego, California, July, 1996.

[5] D. Chichka and J. Speyer, "Solar-Powered Formation-Enhanced Aerial Vehicle Systems for Sustained Endurance", *Proceedings of the 1998 American Control Conference*, Philadelphia, Pennsylvania, June 1998.

[6] Meir Pachter, John J. D'Azzo, and Andrew W. Proud, "Tight Formation Flight Control", *AIAA Journal of Guidance, Control, and Dynamics*, Vol. 24, No. 2, March-April 2001, pp. 246-54.

[7] M. LeBlanc, "Sur l'electrification des chemins de fer au moyen de courants alternatifs de frequence elevee", in *Revue Generale de l'Electricite*, France, 1922.

[8] K. Åström and B. Wittenmark, *Adaptive Control,* Addison Wesley, Reading, Mass., 1989.

[9] M. Krstić and H-H. Wang, "Design and Stability Analysis of Extremum Seeking Feedback for General Nonlinear Systems", *Proceedings of the 36th Conference on Decision and Control*, San Diego, CA, December 1997.

[10] H-H. Wang, S. Yeung, and M. Krstić, "Experimental Application of Extremum Seeking on an Axial-Flow Compressor", *Proceedings of the American Control Conference*, Philadelphia, PA, June 1998

[11] Andrzej Banaszuk, Youping Zhang, and Clas A. Jacobson, "Adaptive Control of Combustion Instability Using Extremum Seeking", *Proceedings of the American Control Conference*, Chicago, Illinois, June, 2000, pp. 416-22.

[12] Gregory C. Walsh, "On the Application of Multi-Parameter Extremum Seeking Control", *Proceedings of the American Control Conference*, Chicago, Illinois, June, 2000, pp. 411-15

[13] Mario Rotea, "Analysis of Multivariable Extremum Seeking Algorithms", *Proceedings of the American Control Conference*, Chicago, Illinois, June, 2000, pp. 433-37

[14] Krishnamurty Karamcheti, *Principles of Ideal-Fluid Aerodynamics*, Robert E. Krieger Publishing Company, Malabar, Florida, 1980.

[15] Joseph Katz and Allen Plotkin, Low-Speed Aerodynamics; From Wing Theory to Panel Methods, McGraw-Hill, New York, NY 1991.

[16] Jan Roskam, *Aircraft Dynamics and Control*, Roskam Aviation and Engineering Corporation, Ottawa, Kansas, 1979, second printing.

[17] Ihnseok Rhee and Jason Speyer, "Application of a Game Theoretic Controller to a Benchmark Problem", *AIAA Journal of Guidance, Control and Dynamics*, Vol.15, No.5, Sep-Oct 1992, pp.1076-1081.

[18] Bernard Friedland, *Control System Design*, McGraw Hill, 1986

[19] Donald Gustafson and Jason Speyer, "Linear Minimum Varience Filters Applied to Carrier Tracking," *IEEE Trans. on Automatic Control*,Vol.AC-21, No.1, February 1976, pp.65-73.

[20] D.F. Chichka, J.L. Speyer and C.G. Park, "Peak-Seeking Control with Application to Formation Flight", *Proceedings of the 38th Conference on Decision and Control*, Phoenix, AZ, December 1999.